scientific reports

Check for updates

OPEN

Numerical and experimental study on the relationship between pull-out force and indentation depth of aviation wire crimp terminal

Pin Li[1], Gongping Liu[3,4], Ping Wang[3,4], Guangwen Huang[3,4], Zhuonan Yu[1], Hang Xiu[1] & Chunlin Tian[1,2]✉

To study the numerical relationship between the pull-out force and indentation depth of aviation wire crimp terminal, the crimping process between electrical contacts and stranded conductors and the tensile process of crimping assembly were simulated by the explicit dynamic finite element method. Regarding the variation trend of the tension of the crimping assembly with the tensile displacement during the tensile process and the failure mode, the numerical results and the experimental results showed a high degree of fit, and the relative error of the pull-out force was only 2.6%, which verified the reliability of the established numerical model. This model obtained the pull-out force curve of the crimp terminal that changes with the indentation depth. The authors suggest selecting the interval where the pull-out force is not less than 95% of the peak value, and the depth is less than the corresponding value at the peak value as the best value range of the indentation depth.

The reliability requirements of aviation wire crimp terminals are extremely high and demanding. Once they fail, the huge losses caused will be irreparable. In the failure rate statistics of American aerospace, the proportion of electrical connector failures is as high as 10%, and about 50–60% of them are directly caused by the failure of the electrical performance of the crimp terminal[1–3]. The connection of dissimilar metal materials has always been a difficult problem in the industry. Different from the more commonly used methods such as riveting and adhesive bonding[4,5], the electrical connection between aviation electrical contacts and wire conductors mainly adopts the four-indenter-eight-indentation crimping method shown in Fig. 1. The evaluation of the electrical performance of the crimp terminal is mainly reflected in two aspects: the pull-out force and the local voltage drop[6,7]. Their measured values are mainly related to three independent factors: the crimping component material, the indenter shape, and the indentation depth[8]. In recent years, in the face of the increasingly diverse characteristics of crimping component materials, the difference in indentation depth required for specific combinations of wires and electrical contacts of the same size and different materials has become more prominent. Traditional crimping tools have been unable to meet aviation wire ends' high-quality, multi-adaptability processing requirements. Therefore, it is essential to explore the method of determining the optimal indentation depth required for a specific combination of electrical contacts and wires to develop intelligent crimping equipment.

At present, the exploration of the crimping mechanism between electrical contacts and wires is mainly based on two methods: theoretical derivation and numerical simulation. For the former, in the previous work[9] of the author of this paper, the mathematical model of the relationship between the pull-out force and the indentation depth of the aviation wire crimp terminal was derived from a 2D perspective. Within a reasonable indentation depth range, the pullout resistance values exhibited by the model are in good agreement with the experimental results. However, the model does not apply when the terminal is in an over-crimped state, which results in the model being unable to represent the optimal indentation depth for the crimping group numerically directly.

[1]School of Mechanical and Electrical Engineering, Changchun University of Science and Technology, Changchun 130022, China. [2]Changchun University of Science and Technology Chongqing Research Institute, Chongqing 401135, China. [3]AVIC Xi'an Aircraft Industry (Group) Company LTD, Xi'an 710089, China. [4]These authors contributed equally: Gongping Liu, Ping Wang and Guangwen Huang. ✉email: 48851795@qq.com

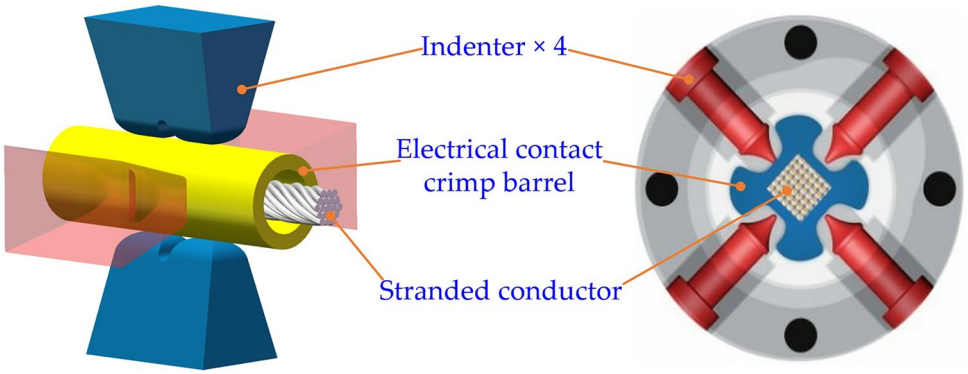

Figure 1. Four-indenter-eight-indentation crimping method for aviation electrical contacts.

Compared with theoretical derivation, the numerical simulation method is more prevalent in many types of research because of its simple and intuitive characteristics.

A high capability of computer analysis and modeling is usually required to simulate the elastic–plastic deformation process. Therefore, to simplify the calculation cost, the initial more research work tends to simulate the dynamic crimping process between the electrical contact and the wire conductor from a 2D perspective. Among them, Kugener[10] took the lead in simulating the crimping process of open-barrel electrical contacts based on the plane stress assumption method by creating a deformable body to represent the multi-core conductor and its sheath as a whole. Due to the existence of gaps inside the actual multi-core conductor, to keep the simulation results consistent with the actual ones, Young's modulus of the imaginary conductor has to be reduced for reference compared to the real conductors. Compared with Kugener's work, Morita[11] carried out the crimping simulation based on the plane strain assumption method. The author found that the simulated crimping force would be greatly increased under this method. Abbas[12] pointed out in his paper that the plane strain assumption method is unsuitable for crimping simulation because the possibility of the material being extruded out of the plane must be ignored in the simulation process. In the study of the four-point crimping method, Lorrière[13] compared the above two 2D plane hypothetical simulations with 3D simulations and concluded that the 3D simulation is the only correct method to simulate crimping. Mocellin[14], Petitprez[15], and others conducted 2D and 3D simulations of the crimping process of aviation closed-barrel electrical contacts for the first time. Through comparison with experiments, they pointed out that the 2D method can only give approximate results, and ignoring the plastic flow of the crimped material in the third direction would lead to an over-constrained model.

Crimping is a quasi-static but highly nonlinear problem, and its corresponding time-integral solving algorithms in simulation usually include two types: implicit and explicit. Since the crimping process involves complex multi-body contact between the crimping barrel and the wire conductor and elastic–plastic deformation of the components, the implicit algorithm usually shows lower efficiency for this situation, so many scientists prefer the explicit algorithm[10–13,16–19]. Among them, Zhmurkin[16,17] used the 3D nonlinear explicit dynamic finite element method to numerically simulate the open-barrel crimping process of 7-core stranded conductors, the effects of the elastic spring-back the components after unloading and geometric parameters of the serrated structure of the crimping barrel on the crimping quality were studied. To study the effects of design variables such as crimping height, crimping width, and crimping die shape on the compression ratio of multi-core stranded conductors, Kim et al.[18,19] carried out 2D and 3D explicit finite element simulations of the crimping process of open-barrel electrical contacts. It is worth noting that the study of Petitprez et al.[20–23], on the premise that they have been convinced that the explicit finite element model can better solve the multi-domain contact problem, the finite element software based on an implicit algorithm was used to inverse analyze the performance parameters of the crimping material. Then, based on this parameter, the same software was used to simulate the crimping of aviation electrical contacts and the tensile process of the crimping assembly. The results show that although the calculation time is very long, this method can also effectively predict the effect of the performance parameters, size, and indentation depth of the crimping material on the mechanical properties of the crimp terminal. Nevertheless, to realize the accurate production of high-quality aviation wire crimp terminals by a new generation of crimping equipment, the specific numerical relationship between the pull-out force and indentation depth of the crimp terminal still needs to be deeply studied.

In this paper, based on the explicit dynamic finite element technology, the numerical simulation of the crimping process between aviation electrical contacts and wires and the tensile process of the crimping assembly was carried out. In terms of the shape, pull-out force, and tensile failure mode of the crimp terminal, the numerical results were compared with the experimental results to verify the reliability of the established numerical model. We further studied the specific numerical relationship between the pull-out force and the indentation depth of the crimp terminal. The selection criteria for the optimal indentation depth range were analyzed and given.

Dynamic finite element simulation theoretical background

Implicit and explicit algorithms applied to models. The implicit algorithm is generally applied to the analysis of static and quasi-static problems, and its time integral form at time t can be expressed as follows:

$$[M]\{a_t\} + [C]\{v_t\} + [K]\{u_t\} = \{F_t\}, \tag{1}$$

where $[M]$ is the mass matrix, $[C]$ is the damping matrix, $[K]$ is the stiffness matrix, $\{a_t\}$ is the acceleration vector, $\{v_t\}$ is the velocity vector, $\{u_t\}$ is the displacement vector, and $\{F_t\}$ is the external force vector. If inertial effects ($[C]$ and $[M]$) are not considered, at time $t+\Delta t$, Eq. (1) can be expressed as follows:

$$\{u_{t+\Delta t}\} = [K]^{-1}\{F_{t+\Delta t}\}. \tag{2}$$

For nonlinear problems, Eq. (2) can be solved for displacement and average external force at time $t+\Delta t$ by a series of linear approximations (*Newton–Raphson* iterations) based on small time steps. However, for highly nonlinear problems, implicit algorithms often fail to guarantee solution convergence.

The explicit algorithm generally first obtains the acceleration value at time t, and then further obtains the velocity and displacement value of the corresponding time step based on the central difference method. The explicit time integration form is as follows:

$$\{a_t\} = [M]^{-1}\left(\left[F_t^{ext}\right] - \left[F_t^{int}\right]\right), \tag{3}$$

where F_t^{ext} is the vector of applied external force and physical force, and F_t^{int} is the internal force vector.

The velocity and displacement of nodes can be obtained by the following Eqs. (4) and (5), respectively:

$$\left\{v_{t+\Delta t/2}\right\} = \left\{v_{t-\Delta t/2}\right\} + \{a_t\}\Delta t_t, \tag{4}$$

$$\{u_{t+\Delta t}\} = \{u_t\} + \left\{v_{t+\Delta t/2}\right\}\Delta t_{t+\Delta t/2}, \tag{5}$$

where $\Delta t_{t+\Delta t/2} = 0.5(\Delta t_t + \Delta t_{t+\Delta t})$. Then, the new geometric configuration can be obtained by adding the displacement increment to the initial configuration, as follows:

$$\{x_{t+\Delta t}\} = \{x_0\} + \{u_{t+\Delta t}\}. \tag{6}$$

For nonlinear analyses, although the explicit algorithm does not require convergence checks, smaller time steps are still necessary for the computation to remain stable. In general, the time step for which the computation is guaranteed to converge must satisfy the following equation:

$$\Delta t \le \Delta t_{cr} = \frac{2}{\omega_{\max}}, \tag{7}$$

where $\omega_{\max}$ is the highest natural vibration frequency of the system, and its value is generally determined by the smallest element in the corresponding configuration mesh at each moment.

Correction of stress–strain function. Typically, the nominal stress–strain function can be obtained by standard tensile or compressive experiments as follows:

$$\sigma_e = \frac{F}{S_0} = f(\varepsilon_e), \tag{8}$$

where σ_e is the nominal stress, ε_e is the nominal strain, $\varepsilon_e = (L - L_0)/L_0$, L_0 is the initial length, F is the normal force, and S_0 is the initial cross-sectional area. However, when the material is in a state of non-uniform plastic deformation, local necking will occur, resulting in an inconsistent cross-sectional area of the overall material. Therefore, the nominal stress–strain function is reasonably accurate for small deformation analysis but unacceptable for realistic, in-depth mechanical engineering analysis.

Facing the above problems, Francois et al.[24] corrected the nominal stress–strain function based on the first-order approximation by assuming that the material volume is conserved. The nominal values of stress and strain measured by experiments are converted into real values that can be used in practical engineering problems. The correction equations are as follows:

$$\sigma_t = \sigma_e(1 + \varepsilon_e) \tag{9}$$

$$\varepsilon_t = ln(1 + \varepsilon_e), \tag{10}$$

where σ_t and ε_t are the true stress and strain values at time t, respectively.

However, it is very difficult to obtain the completely true stress–strain relationship function of materials in practical engineering. To simplify the simulation workload, usually, we can first use the above correction equations to convert the material properties such as yield strength σ_s, tensile strength σ_b, Young's modulus E, elongation δ provided by the manufacturer into the true yield strength σ_{s_t}, yield strain ε_{s_t}, tensile strength σ_{b_t}, and tensile strain ε_{b_t}. Then, the bilinear estimation method is used to simplify the true stress–strain relationship function of the material. The first stage of the bilinear is elastic, and the slope is Young's modulus E; the second stage is plastic, and the slope is the tangent modulus E_T, and its value can be obtained by the following equation:

$$E_T = \frac{\sigma_{b\_t} - \sigma_{s\_t}}{\varepsilon_{b\_t} - \varepsilon_{s\_t}} \tag{11}$$

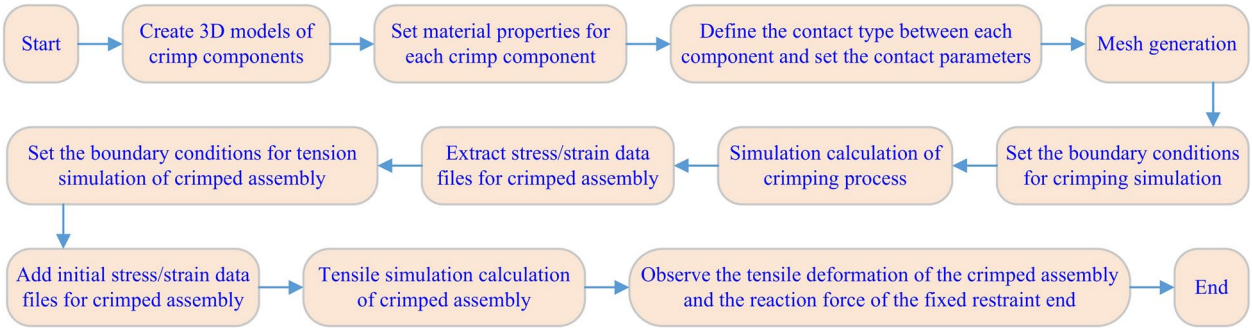

Figure 2. The flow of the overall simulation work.

Definition of contact interface. In dynamic finite element simulation, there are usually three types of model interface contact: single-face, point-to-face, and face-to-face. Among them, the single-face contact type is the most popular for situations where the model is cumbersome and the contact state is unpredictable. The reason for this is that with this type when the program checks whether the models penetrate each other, all outer surfaces are within the search range, so there is no need to specifically define the contact surface and target surface where contact may occur.

The good handling of the contact interface is inseparable from a reasonable contact control algorithm. For common sliding contacts, the "symmetric penalty function" method is the most commonly used algorithm. The basic principle is that, based on a contact search algorithm and a dual-loop master–slave algorithm for determining normal and tangential forces[25], the program sequentially verifies the contact compatibility of each node in the model at each time step. Because the algorithm has symmetry and does not require collision and release conditions, it rarely causes the hourglass effect and can accurately ensure the conservation of momentum of the system.

In the dynamic finite element simulation, the friction coefficient μ_c is composed of the static friction coefficient μ_s, the dynamic friction coefficient μ_d, and the exponential decay coefficient β. It is considered that with the increase of the relative velocity V_{rel} of the contact surface, the value of the friction coefficient μ_c decays exponentially from μ_s to μ_d, as shown in the following equation:

$$\mu_c = \mu_d + (\mu_s - \mu_d)e^{-\beta \cdot V_{rel}}. \tag{12}$$

In addition, the maximum friction force $F_{\max}$ can be defined by the viscosity coefficient V_c:

$$F_{max} = V_c \cdot A_{cont}, \tag{13}$$

where A_{cont} is the contact area, it is recommended that $V\_c = \sigma\_s/\sqrt{3}$, and σ_s is the yield stress of the contacting material.

Dynamic Saint–Venant's principle. Numerous studies have confirmed the application of Saint–Venant's principle (SVP) to dynamic problems. For the dynamic finite element simulation of nonlinear metal local forming, the calculation results should fully consider the boundary effect based on SVP. Karp[26] gave a dynamic interpretation of the SVP and believed that whether the structure satisfies the dynamic SVP depends on the following two conditions:

(1) The dynamic resultant force of the external load is zero;
(2) The stress wave excited by the external load in the structure has zero effect on the far end of the system.

The energy flow carried by the stress wave propagating in space is generally considered a measure of wave intensity. The derivation of the energy flow can be expressed as follows[27]:

$$P = \frac{1}{2} G d \xi \frac{\omega^3}{C_T} A^2, \tag{14}$$

where, P is the energy flow, G is the shear modulus, d is the thickness of the propagation medium, ξ is the wave number, ω is the frequency, A is the amplitude, and C_T is the phase velocity of the shear wave.

Pre-processing of aviation electrical contact crimping simulation

In this study, we used the LS-DYNA module under the CAE software ANSYS™ to calculate the crimping process and the crimped assembly's tensile process. LS-DYNA is a nonlinear dynamic finite element analysis program based on explicit algorithms, which is especially suitable for solving nonlinear metal forming problems in quasi-static mode. Figure 2 shows the flow of the overall simulation. Next, let's introduce the pre-processing work of crimping simulation.

Crimping model and material properties. Figure 3A shows the overall 3D simulation model, including the indenter. Unlike previous crimping simulation studies, the stranded conductor model preserves the twisting

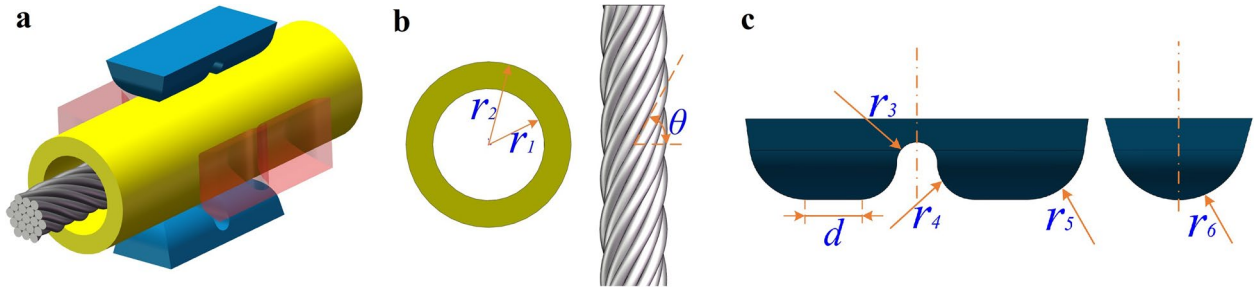

Figure 3. 3D crimping simulation model construction and dimension setting. (**a**) 3D crimping simulation model; (**b**) electrical contacts and stranded conductors; (**c**) crimping action part of the indenter.

r_3	r_4	r_5	r_6	d
0.15	0.28	0.42	0.5	0.4

Table 1. Relevant design dimensions of the crimping action part of the indenter (*mm*).

	ρ (g · cm^{-3})	E (MPa)	$\sigma_{0.2}$(MPa)	σ_b(MPa)	δ (%)	ν
Crimping barrel	8.3	1.28 × 105	483	552	25	0.35
Stranded conductor	8.96	1.24 × 105	90	200	30	0.34

Table 2. Relevant mechanical properties of crimping components.

characteristics of actual multi-core strands. Even though this would prevent the overall model from being symmetrically simplified, the simulation results would be more realistic.

According to the adaptation requirements of the size specification between the electrical contact and the stranded conductor in the standard *SAE-AS39029*[28] document, 20# electrical contacts and 22*AWG* 19-core stranded conductors were selected as the basis for dimensioning the crimping component model. As shown in Fig. 3b, the diameter of a single core in the strand is 0.15 *mm*, the twist angle θ is 60°, the inner surface radius r_1 of the electrical contact crimping barrel is 0.6 *mm*, and the outer surface radius r_2 is 0.89 *mm*. Figure 3(c) shows the morphology of the crimping part of the indenter, and Table 1 lists the relevant design dimensions according to the design specification requirements of the stamper in the standard *SAE-AS22520* document[29].

According to the regulations on the material properties of crimping components in the standard *SAE-AS39029* document, the material for the crimping barrel of the aviation electrical contact is C17200 beryllium copper, and the material for the aviation stranded conductor is traditional oxygen-free copper. Their density ρ, Young's modulus E, Poisson's ratio ν, yield strength $\sigma_{0.2}$, tensile strength σ_b, and elongation δ are listed in Table 2, respectively. In addition, the stamper is generally made of cemented carbide steel material with high hardness, high bearing capacity, and strong wear resistance, which has an excellent ability to resist deformation. Therefore, in the process of crimping simulation, the stamper was treated as a rigid object to simplify the calculation.

Contact definition and meshing. The crimping of aviation electrical contacts is a multi-domain extrusion contact problem, and the possible contact positions are relatively ambiguous. Therefore, the overall model adopted the single-face contact type introduced in Section "Definition of Contact Interface", avoiding defining unknown contact surfaces and target surfaces. In addition, for the extrusion contact problem, mutual penetration between the model surface nodes is not allowed during the simulation process. Using the "symmetric penalty function" method introduced in Section "Definition of Contact Interface" as the contact control algorithm for the overall model can effectively solve this problem. At the same time, the algorithm can also significantly reduce the zigzag contact deformation caused by the hourglass effect[30]. Referring to the research of Kim et al.[19], the static friction coefficient of the crimping barrel-wire core contact, the crimping barrel-indenter contact, and the crimping barrel self-contact is set to 0.2. The static friction coefficient of the contact between the wire cores is set to 0.15, the dynamic friction coefficient of all contacts is set to 0.1, and the decay coefficient is set to 1 by default.

As shown in Fig. 4, the overall model adopted two meshing methods. Applying a tetrahedral mesh to indenter models with relatively complex structural features will make it easier to automatically refine the mesh in critical areas using curvature and approximate size functions. Applying a hexahedral mesh at the same density as the tetrahedral mesh will exhibit fewer elements and nodes. Therefore, we used the hexahedral mesh to the crimping barrel and stranded conductor models based on the sweep method to obtain a more regular and uniform mesh distribution. In addition, considering the calculation accuracy, it is necessary to perform mesh refinement on the indenter-crimping barrel contact area and the crimping barrel-stranded conductor contact area. At the same time, to balance calculation accuracy and time, the rationality of mesh refinement needs to be verified. Generally,

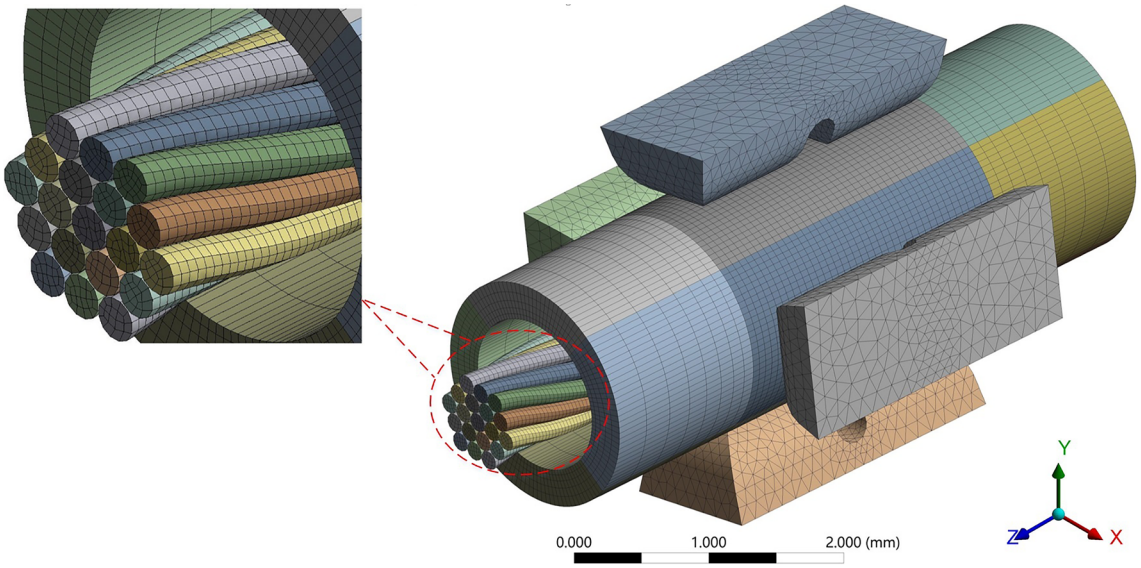

Figure 4. Meshing of the crimping model.

Contact area	Minimum element size (*mm*)				
Indenter-crimping barrel	0.04	0.05	0.06	0.07	0.08
Crimping barrel-stranded conductor	0.03	0.035	0.04	0.045	0.05
Number of elements (thousand)	≈240	≈160	≈110	≈85	≈70

Table 3. The number of elements corresponding to different mesh refinement densities.

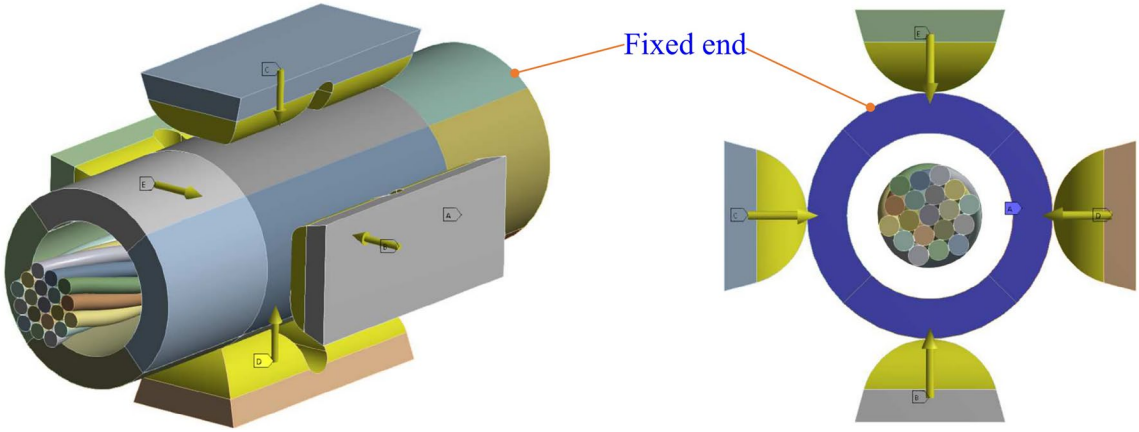

Figure 5. Boundary condition settings for the crimping simulation.

a mesh-independent solution is considered to be obtained when the mesh is refined to have a negligible effect on the results. Here, we set five groups of minimum element size for the above two mesh refinement areas, and Table 3 shows the number of elements corresponding to each group.

Boundary conditions and simulation parameter settings. As shown in Fig. 5, one end of the crimping barrel model was fixed according to the actual crimping operation. The four indenters were set to move vertically and centripetally synchronously. We should establish the moving speed of the indenter concerning the time step of the simulation calculation, which is determined by the size of the mesh element and the longitudinal acoustic wave velocity in the model material[31,32]. As mentioned in Section "Implicit and explicit algorithms applied to models", to obtain numerical stability, the default time step of the system is generally small, which is very unfavorable to the computational efficiency of the simulation of low-speed phenomena such as most metal forming processes. Artificially increasing the material's mass density or the model's mesh size can increase the time step and speed up the analysis process[33,34], but this will also reduce the accuracy of the simulation.

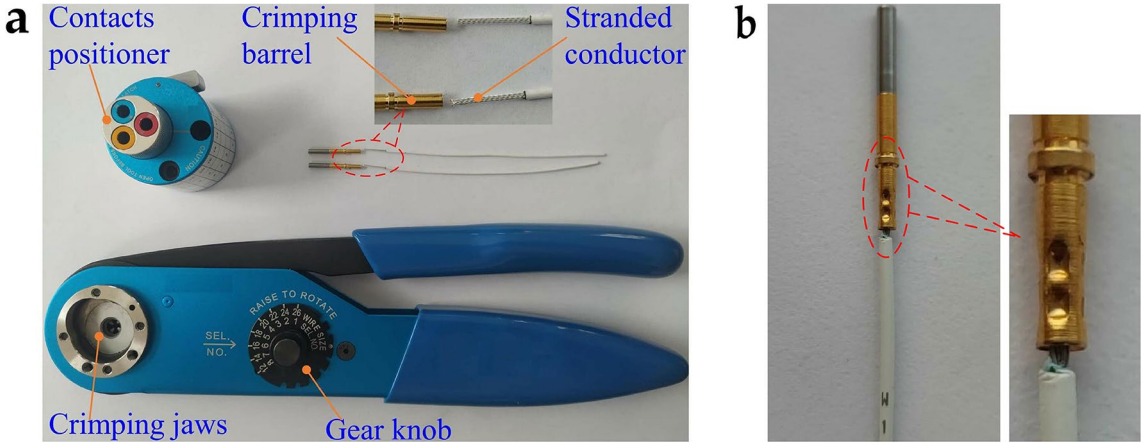

Figure 6. Crimping tools, materials, and crimping samples.

Gear No. (#)	Indentation depth (*mm*)
1	0.4709 ~ 0.5344
2	0.4201 ~ 0.4836
3	0.3693 ~ 0.4328
4	0.3312 ~ 0.3947
5	0.2550 ~ 0.3185
6	0.1661 ~ 0.2296
7	0.0772 ~ 0.1407
8	-0.0371 ~ 0.0264

Table 4. Corresponding indentation depth of 20# electrical contact crimping barrel under each crimping gear.

Reference[10] pointed out that when the inertia effect is negligible, the speed of the die can be increased to speed up the simulation analysis. Typically for an element size of 0.01 *mm*, the default time step Δt is about 10^{-9} s. However, for the crimping process considered in this study, the actual indenter speed is about 0.2 m/*s*, which is very slow for the default time step. Increasing the indenter velocity in the simulation to 1 m/*s* did not result in significant inertial effects.

On the other hand, to improve computational efficiency, the explicit dynamic analysis program usually automatically simplifies the integration unit locally to reduce the number of integration points. However, the simplified integration unit is prone to produce zero-energy modes, which lead to invalid calculation results, namely hourglass modes. Studies have pointed out that for the elastic–plastic deformation problem under solid elements, the "*Belytschko-Bindeman*" method can effectively control the hourglass deformation phenomenon that may occur in the simulation[35,36]. For the elastic–plastic crimp deformation process considered here, the hourglass control factor under this method is set to 0.01 by default.

Experiments

Crimping of electrical contacts. Figure 6A shows the tools and materials used for the crimping experiment. Among them, the electrical contact is a 20# gold-plated beryllium copper alloy contact suitable for *MIL-DTL-38999*I, II, III series military electrical connectors, purchased from Huafeng Electrical Co., Ltd., Guizhou, China. The aviation wire specification is 22*AWG*, and the conductor type is 19-core stranded soft silver-plated copper wire purchased from Quanxin Cable Technology Co., Ltd., Nanjing, China. The crimping pliers (model *YJQ-W2A*) have eight crimping gears and can be used to crimp wires in the range of 12 to 26*AWG*; the electrical contact positioner (model *TH163*) can be used to assist the crimping pliers in fixing 12#, 16#, and 20# contacts. They were all purchased from Jingrui Instrument & Equipment Co., Ltd., Jiaxing, China.

By adjusting the crimping gear to change the feed displacement of the indenter, we can change the indentation depth of the crimping barrel. The manufacturer-provided design documents gave the indenter feed displacement corresponding to each crimping gear. Based on this, according to the outer diameter of the 20# electrical contact crimping barrel, the indentation depth corresponding to each crimping gear can be determined, as shown in Table 4. It can be seen that only in the 1 ~ 5# gear will there be an extrusion effect between the crimping barrel and the stranded conductor. Therefore, in this experiment, only crimping samples were made in the 1 ~ 5# gear, and five pieces were made in each gear. Figure 6b shows the crimping example.

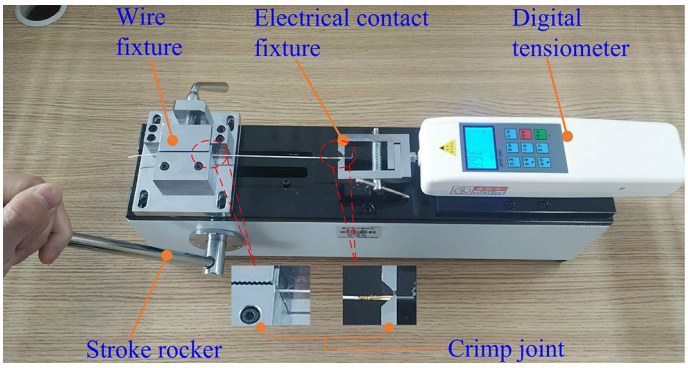

Figure 7. Pull-out force detection of crimp terminals.

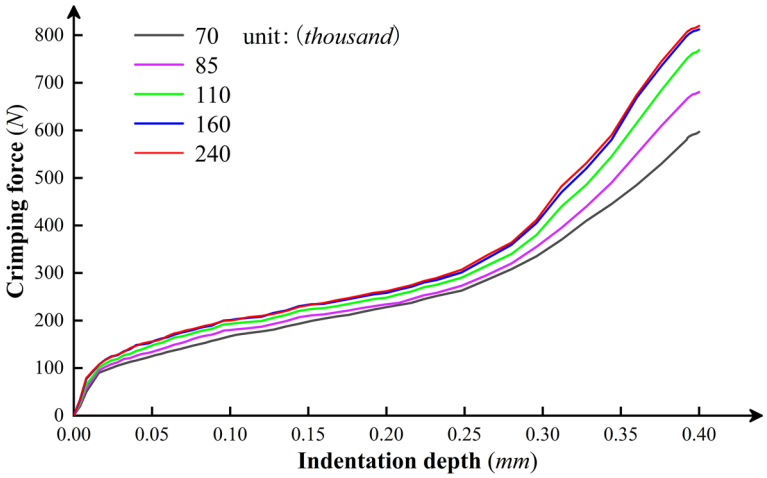

Figure 8. Crimping force curve as a function of the indentation depth under different numbers of mesh elements.

Pull-out force test of crimp terminals. The terminal pull-out force tester was purchased from Xiangbang Automation Equipment Co., Ltd., Shenzhen, China, with a maximum load of 500 *N*, an accuracy of 0.1 *N*, and a test range of 50 *mm*.

The detection method of the pull-out force of the crimp terminal is shown in Fig. 7. After assembling the terminal pull-out force tester, fix one end of the electrical contact of the crimping sample to the right fixture and one end of the wire to the left institution, and keep the sample horizontal. Set the digital tensiometer to the "Maximum" mode, turn the stroke rocker to move the left fixture to the left at a speed of about 25 *mm/min*, and record the failure type of each sample and the maximum tension value after failure.

Results and discussion

Mesh verification. During the verification process, we set the indentation depths under different mesh densities to 0.4 mm, and other constraints and loading conditions were kept unchanged. In the crimping simulation, by capturing the indenter's normal contact force data acting on the crimping barrel's surface at each time node, the crimping force curve shown in Fig. 8 as a function of the indentation depth under different numbers of mesh elements could be obtained. Generally, if the relative error between the numerical solutions at adjacent two groups of mesh element numbers is less than 5%, the effect of mesh on the results is considered acceptable. It can be seen that when the number of elements is below 160,000, the change in mesh density has a high impact on the calculation results. However, with a further increase in the number of elements, the fit of the crimping force curve is better, and the sensitivity of the calculation results to the mesh is negligible. Therefore, it is reasonable to select the mesh refinement element size corresponding to the number of mesh elements of 160,000 for the crimp simulation.

Comparison between experiment and simulation

Crimping effect. In the user manual of the crimping plier, it is recommended to select the 3# gear to crimp the specific combination of 20# electrical contacts and 22*AWG* aviation wires. Figure 9a shows the crimping simulation deformation results under the middle value (0.4 *mm*) of the indentation depth range corresponding

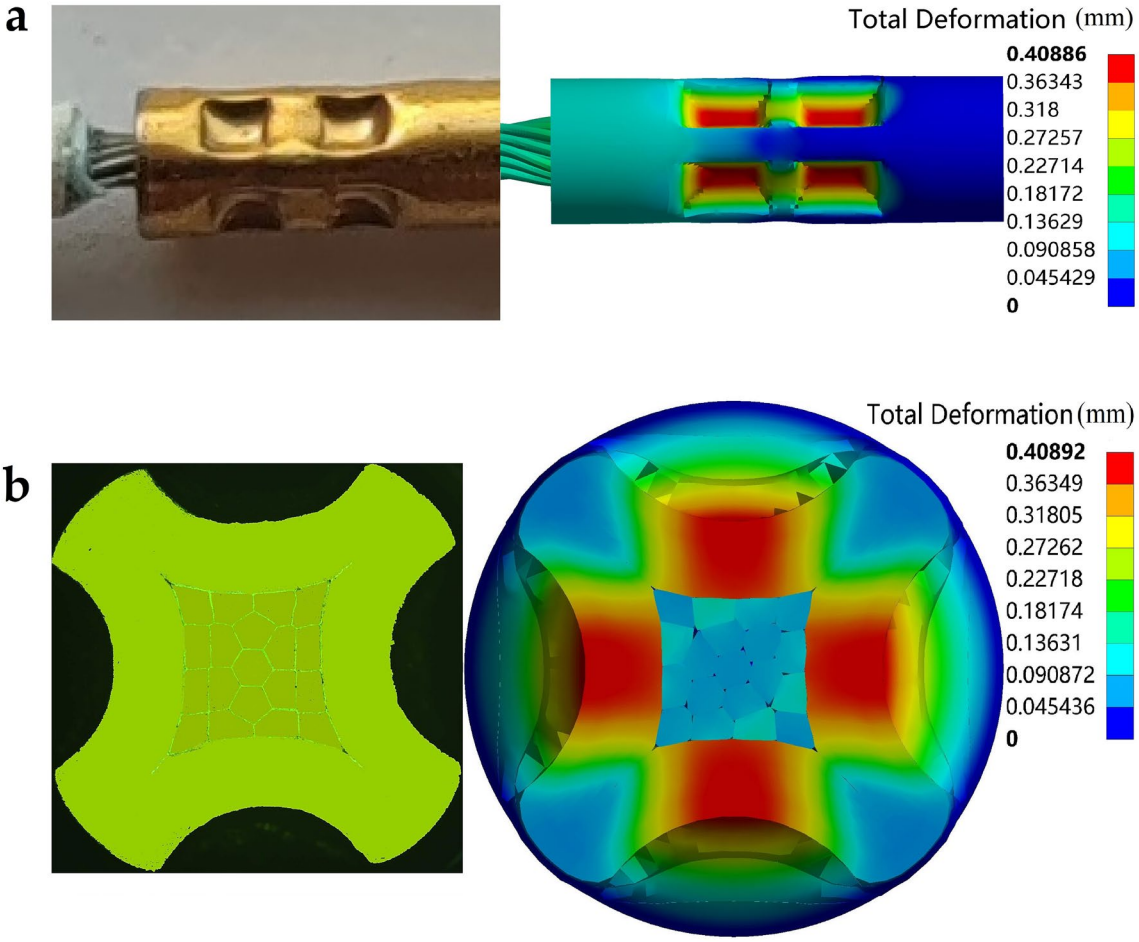

Figure 9. Comparison of crimping assembly geometries in experiment and simulation.

to the 3# gear. Compared with the real crimping assembly in the 3# gear, it can be seen that the geometric shapes of the two are the same. At the same time, metallographic microscopic analysis was carried out on the radial deformation of the cross-section of the crimped part of the sample, as shown in Fig. 9b. In the corresponding numerical results, although there are some slight gaps inside the compressed stranded conductor, after the load of the indenter is released, the stranded conductor and the inner wall of the crimping barrel still maintain a complete extrusion state. Therefore, these small gaps do not have a substantial impact on the subsequent simulation results of the crimp terminal pull-out force.

The ratio of hourglass energy to internal energy (RHI) can be used to examine the system's energy balance that may be disrupted by hourglass control. Several studies on elastic–plastic contact deformation simulation have given a basic standard of RHI value that can determine the computational quality[37–39]. The RHI value after the simulation should not be greater than 10%. Figure 10a shows the curves of the system's internal and hourglass energy as a function of indentation depth during the crimping simulation. Figure 10b indicates that the RHI value of the simulation process is lower than 2.5%, and the final value is about 2%. It suggests that the system energy during the crimping simulation process is balanced, and the calculation accuracy is high. At the same time, this also verifies the rationality of the contact definition, meshing, and hourglass control type selection of the overall crimping model in Sections "Contact Definition and meshing" and "Boundary conditions and simulation parameter settings".

Pull-out force and tensile failure mode of crimp terminals. According to standard *SAE-AS22520*, for the specific combination of 20# electrical contact and 22*AWG* aviation wire, the pull-out force of the crimp terminal shall not be less than 60 *N*. Table 5 records the test values of the pull-out force and the corresponding failure mode of the crimp terminal samples under the 1 ~ 5# crimping gears in the experiment. When the 1# and 5# gears were selected, since the assemblies were in two states of over-crimping and under-crimping, respectively, the pull-out force of the corresponding crimping sample did not meet the standard requirements at all. For the tensile failure mode of the crimp terminal, the former showed that the stranded conductor was easily broken at the crimping part, and the latter showed that the stranded conductor slipped out of the electrical contact. In addition, when the 4# gear was selected, the failure mode was that the stranded conductor was partially broken at the crimping

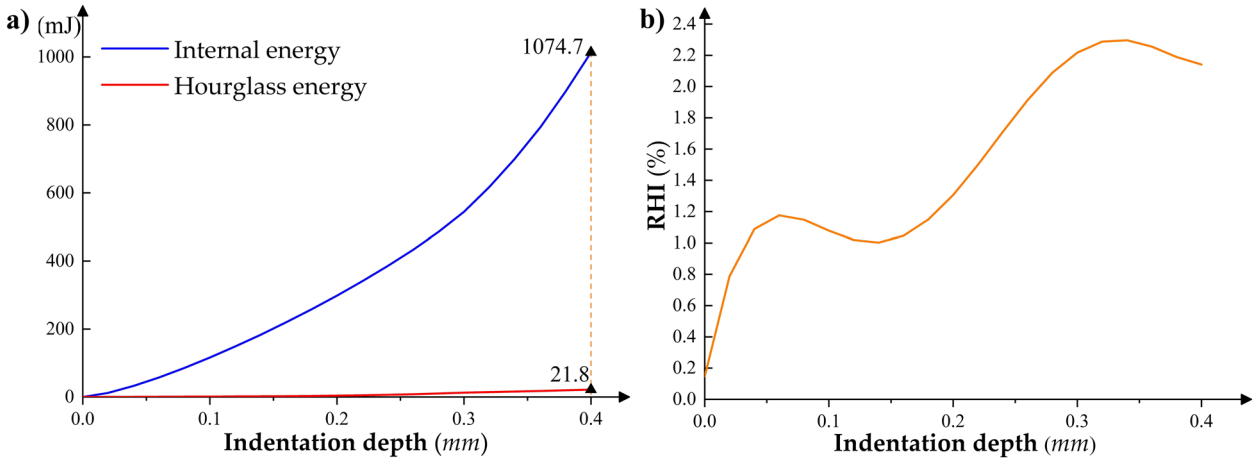

Figure 10. Variation of system energy with indentation depth during crimping simulation. (**a**) Internal energy and hourglass energy; (**b**) The "RHI" value as a function of indentation depth.

Gear No. (#)	Pull-out force (*N*)	Failure mode
1	42.7/40.5/43.6/39.7/40.1	Strands breakage
2	72.1/70.3/69.8/73.1/71.5	Strands breakage
3	83.3/82.5/81.9/81.3/82.5	Strands breakage
4	72.1/70.5/68.7/69.3/70.6	Partial breakage of strands
5	33.3/36.1/31.8/32.7/35.1	Strands slippage

Table 5. Pull-out force and failure mode of crimping samples under different crimping gears.

part, and part of the wire core slipped out of the electric contact crimping barrel. Although the pull-out force of the crimp terminal did not reach the optimal value, it still met the standard requirements.

Select the indentation depth range's median value (0.5 *mm*, 0.45 *mm*, 0.4 *mm*, 0.36 *mm*, and 0.29 *mm*, respectively) corresponding to 1 ~ 5# gear for crimping simulation. Then, based on the sequential coupling method, one end of the stranded conductor of the crimping assembly model with the stress–strain results was set to a fixed state, and a certain displacement was added to one end of the electrical contact, which can realize the simulation of the pull-out force and failure mode of the crimp terminal. Here, for crimping components without apparent yield plateau, such as copper and copper alloys, the tensile failure state of the material can be approximately represented by tensile strain at break instead of elongation at break[40]. Figure 11 shows the tensile simulation results, and we can find that the numerical results at each indentation depth are in good agreement with the experimental results shown in Table 5 for the pull-out force and tensile failure mode of the crimp terminal. Among them, it is worth noting that at the indentation depth corresponding to gears 1# (Fig. 11a) and 2# (Fig. 11b), the stranded conductors are locally crushed at the crimping position, which is not advisable.

In the tensile simulation, we can obtain the tension of the crimping assembly by capturing the opposing force at the fixed end of the stranded conductor at each time node. Here, to further verify the reliability of the tensile simulation results of the crimping assembly, the relationship between the tension and the traction displacement in the tensile simulation results at the indentation depth corresponding to the 3# crimping gear was compared with the one in the experimental results. Figure 12 superimposed the force–displacement curves of the tensile simulation and multiple sets of tensile tests, and the average experimental data curve was also plotted. We can find that before the crimp terminal failed, the force–displacement trends in the practical and simulated results were the same. The overall experimental data has low dispersion, and the relative error between each group of experimental data and the average data is less than 3.4%. Moreover, the relative error between the simulation data and the experimental average data is less than 2.6%, which is enough to show that the established tensile simulation model of the crimping assembly has high computational accuracy. After failure, the stranded conductor gradually slipped out of the crimping barrel due to partial breakage, resulting in an oscillation phenomenon in the pull-out force simulation data.

Determination of optimal indentation depth range. Based on the tensile simulation results of the crimping assemblies in Section "Pull-Out Force And Tensile Failure Mode Of Crimp Terminals", the optimal indentation depth range for the specific combination of 20# electrical contacts and 22*AWG* aviation wires can be initially narrowed to within 0.36 ~ 0.45 *mm*. Then, within this range, a series of crimping and assembly tensile strength simulations were carried out with 0.005 mm as the indentation depth increment, and the variation of crimp terminal pull-out force and its failure mode with indentation depth was obtained, as shown in Fig. 13. It

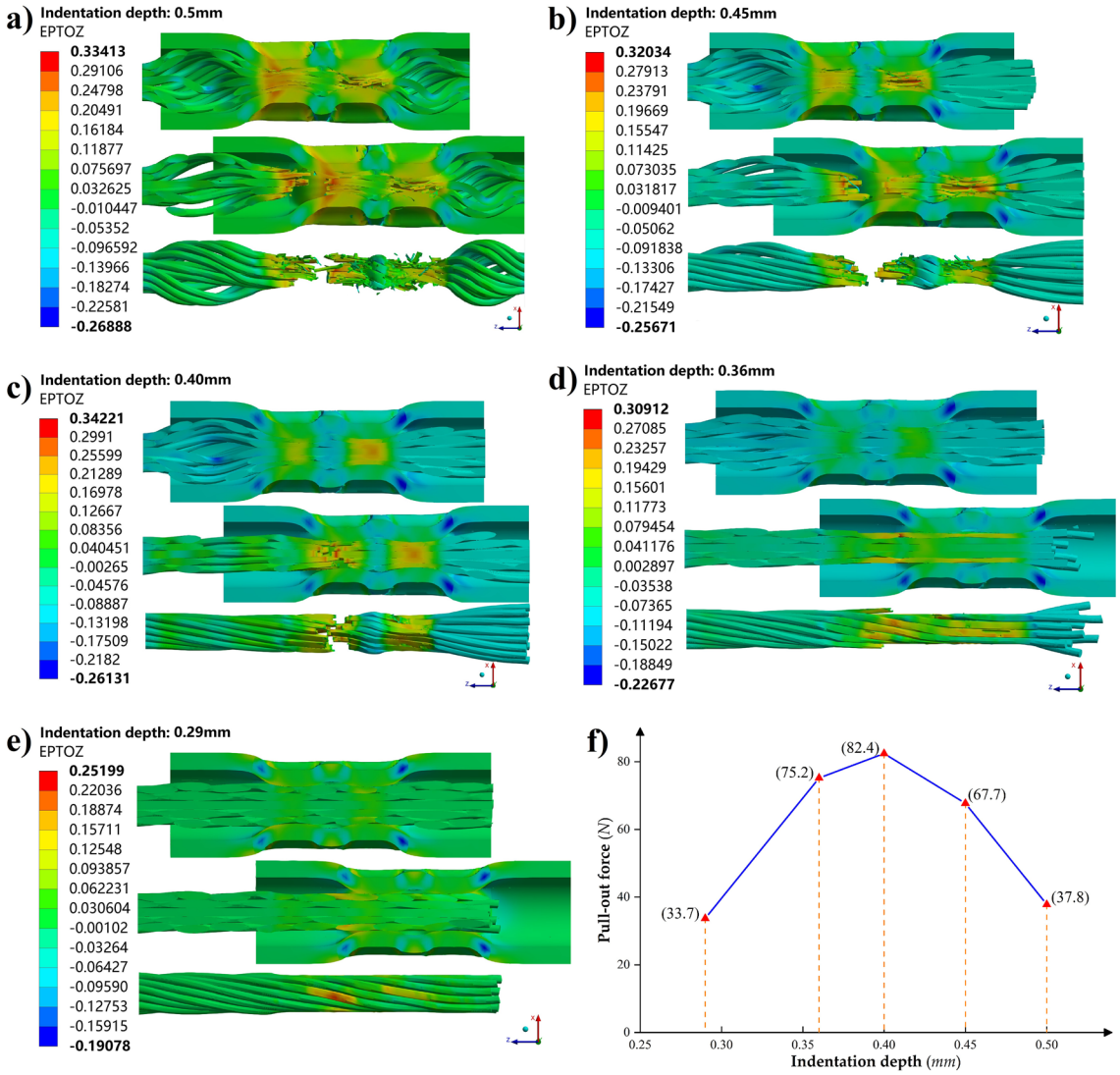

Figure 11. Tensile simulation results of the crimping assembly at the indentation depth corresponding to the 1 ~ 5# gear. The indentation depths are respectively taken as: (**a**) 0.5 mm; (**b**) 0.45 mm; (**c**) 0.4 mm; (**d**) 0.36 mm; (**e**) 0.29 mm. (**f**) The pull-out force of crimp terminals for each indentation depth.

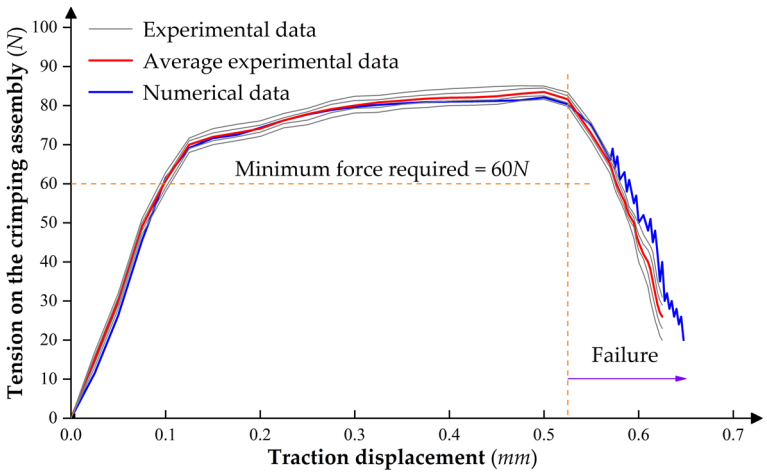

Figure 12. Experimental and simulated force–displacement curves for the tensile strength of the crimping assembly corresponding to the 3# crimping gear.

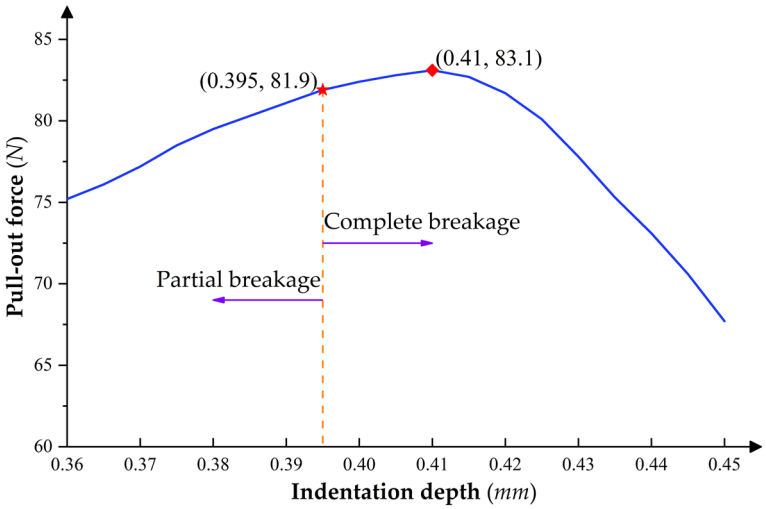

Figure 13. Variation of crimp terminal pull-out force and its failure mode with indentation depth.

can be seen that when the indentation depth is greater than 0.395 *mm*, the stranded conductor begins to show a complete breakage phenomenon at the crimping part, and the indentation depth corresponding to the peak of the pull-out force is also in the complete breakage failure mode region. Therefore, considering the possible dimensional manufacturing errors of the crimping components and the indenter, to avoid over-crimping, the selected indentation depth should be within the range where the pull-out force is not less than 95% of the peak value, and the depth is less than the corresponding value at the peak value. The optimal indentation depth range should be 0.38 ~ 0.41 *mm* for the crimping combinations considered here.

Conclusions

This paper studies the quasi-static multi-domain contact problem of aviation electrical contact crimping by explicit dynamic finite element simulation method based on theoretical analysis. The conclusions are as follows:

(1) The simulation and experimental results on the extrusion deformation of the crimping assembly showed a high degree of fit, and the RHI value of the system after the simulation was only about 2%, which verified the reliability and stability of the established crimping numerical model.
(2) Based on the sequential coupling method, a tensile failure simulation was performed on a crimping assembly model with stress–strain results. The tensile failure modes in the simulation and experimental results were consistent, and the relative error of the pull-out force was only 2.6%, which showed that the established numerical model on the tensile strength of the crimping assembly has high computational accuracy.
(3) For the specific combination of 20# electrical contact and 22AWG aviation wire, the pull-out force curve of the crimp terminal as a function of the indentation depth was obtained, and the optimal indentation depth range corresponding to the combination was analyzed and given.

Data availability

The datasets of related experiments and simulations involved in this article are available from the corresponding author upon reasonable request.

Received: 26 October 2022; Accepted: 16 December 2022
Published online: 19 December 2022

References

1. Lv, J. H., Wang, W. Z. & Liu, S. W. Statistical analysis of failure cases in aerospace. *IJAME* **12**, 497–501. https://doi.org/10.5281/zenodo.1316616 (2018).
2. Tan, C. L. & Hu, T. B. Analysis on foreign spacecraft in-orbit failures. *Spacecr. Eng.* **20**, 130–136. https://doi.org/10.3969/j.issn.1673-8748.2011.04.018 (2011).
3. Zong, Y. List of faults of American space shuttle. *Aerospace China.* **5**, 16–20+24 (2003).
4. Jiang, H. *et al.* Mechanical properties and corrosion behavior of galvanized steel/Al dissimilar joints. *Arch. Civ. Mech. Eng.* **21**, 1–13. https://doi.org/10.1007/s43452-021-00320-5 (2021).
5. Jiang, H. *et al.* Comparative study on joining quality of electromagnetic driven self-piecing riveting, adhesive and hybrid joints for Al/steel structure. *Thin wall struct.* **164**, 107903. https://doi.org/10.1016/j.tws.2021.107903 (2021).
6. Xu, L., Qiu, K. & Li, Y. Failure mode and analysis of aerospace crimping cable. *Aerosp. Manuf Technol.* **4**, 28–31 (2014).
7. Wang, G. Y. Contact crimping technology and control. *China CIO News* **3**, 97+99 (2016).
8. Hayner, N. A. Selecting the proper crimp tool setting for crimp contact—Wire terminations. *Eng. Semin. Electr. Contact Phenom.* 273–286. (1967).

9. Li, P. *et al.* Mathematical model for the tensile strength of the crimping assembly of aviation wiring harness end. *Sci. Rep.-UK* **11**, 17868. https://doi.org/10.1038/s41598-021-97498-8 (2021).
10. Kugener, S. Simulation of the crimping process by implicit and explicit finite element methods. *AMP J. Technol.* **4**, 8–15 (1995).
11. Morita, T. Numerical model of crimping by finite element method. In Proceedings of the 42nd IEEE Holm Conference on Electrical Contacts. Joint with the 18th International Conference on Electrical Contacts, 151–155. https://doi.org/10.1109/holm.1996.557192 (1996).
12. Abbas, M. Modeling and optimization of the crimping of electrical connectors used in the automotive industry. Doctoral dissertation, University of Technology of Compiegne, Compiegne, France, 85–88. (2002).
13. Lorrière, P. et al. Finite element modeling of aeronautical electrical contact crimping. In Proceedings of the 6th National Symposium on structural calculation, 19–25. (2003).
14. Mocellin, K., Petitprez, M. & Desjean, C. Computational Modeling of Electrical Contact Crimping and Mechanical Strength Analysis. In Proceedings of the 56th IEEE Holm Conference on Electrical Contacts, 1–3. https://doi.org/10.1109/holm.2010.5619564 (2010).
15. Petitprez, M., Mocellin, K. & Desjean, C. Study of crimping and mechanical strength of electrical contacts. In Proceedings of the 10th National Symposium on structural calculation, 16–19. (2011).
16. Zhmurkin, D. V., Corman, N. E. & Copper, C. D. 3-Dimensional numerical simulation of open-Barrel crimping process. In Proceedings of the 54th IEEE Holm Conference on Electrical Contacts, Orlando, 178–184. https://doi.org/10.1109/HOLM.2008.ECP.41 (2008).
17. Zhmurkin, D.V. 3-D simulation of open-barrel crimping process: Study of the effect of serrations. In Proceedings of the 55th IEEE Holm Conference on Electrical Contacts, 114–120. https://doi.org/10.1109/HOLM.2009.5284414 (2009).
18. Yin, Z. H., Park, J. G., Choi, H. S. & Kim, Y. S. Quality improvement for crimping process of electrical connector using FEM analysis. *Trans. Mater. Process.* **18**, 229–235. https://doi.org/10.5228/kspp.2009.18.3.229 (2009).
19. Gu, S. M., Choi, H. S. & Kim, Y. S. Effects of design variables on compression rate of wire in connector crimping process of wire harness using FEM. *Trans. Mater. Process.* **19**, 305–310. https://doi.org/10.5228/kspp.2010.19.5.305 (2010).
20. Petitprez, M. & Mocellin, K. Numerical study of a crimped assembly mechanical strength. *Key Eng. Mater.* **554**, 1037–1044. https://doi.org/10.4028/www.scientific.net/kem.554-557.1037 (2013).
21. Mocellin, K. & Petitprez, M. Experimental and numerical analysis of electrical contact crimping to predict mechanical strength. *Proc. Eng.* **81**, 2018–2023. https://doi.org/10.1016/j.proeng.2014.10.274 (2014).
22. Petitprez, M. Numerical simulation of the crimping process for aeronautical electrical contacts: Optimization of assembly conditions for mechanical strength. Doctoral dissertation, National School of Mines of Paris, France. (2013).
23. Petitprez, M. & Mocellin, K. Nonstandard samples behaviour law parameters determination by inverse analysis. *Comput. Methods Mater. Sci.* **13**, 56–62 (2014).
24. Francois, D., Pineau, A. & Zaoui, A. *Elasticity and Plasticity* 201–223 (Kluwer Academic Publishers, 1998).
25. Pichelin, E., Mocellin, K. & Fourment, L. An application of a master-slave algorithm for solving 3D contact problems between deformable bodies in forming processes. *Eur. Rev. Elements.* **10**, 857–880 (2001).
26. Karp, B. Dynamic version of Saint-Venant's principle—Historical account and recent results. *Nonlinear Anal.* **63**, e931–e942. https://doi.org/10.1016/j.na.2005.01.035 (2005).
27. Miklowitz J. The theory of elastic waves and waveguides (ed. Lauwerier, H.) 367–368 (North-Holland, 2012).
28. SAE-AS39029: Crimp Contacts, Electrical Connector, General Specification. (2011).
29. SAE-AS22520: Crimping Tools, Wire Termination, General Specification. (2011).
30. Hu, R. X. & Kang, S. T. Simple Integral and Hourglass in ANSYS 18.0/LS-DYNA (ed. Qu, C. Y.), 27–29. (China Machine Press, 2018).
31. Flanagan, D. P. & Belytschko, T. Eigenvalues and stable time steps for the uniform strain Hexahedron and Quadrilateral. *J. Appl. Mech.* **51**, 35–40. https://doi.org/10.1115/1.3167594 (1984).
32. Pagnacco, E., Lorrière, P. & Dhatt, G. Crimping of aeronautical electrical contacts: modeling, correlation and parametric study. In Proceedings of the 7th national symposium on structural calculation. (2005).
33. Prior, A. M. Applications of implicit and explicit finite element techniques to metal forming. *J. Mater. Process. Tech.* **45**, 649–656. https://doi.org/10.1016/0924-0136(94)90413-8 (1994).
34. Sun, J. S., Lee, K. H. & Lee, H. P. Comparison of implicit and explicit finite element methods for dynamic problems. *J. Mater. Process. Tech.* **105**, 110–118. https://doi.org/10.1016/S0924-0136(00)00580-X (2000).
35. Belytschko, T. & Bindeman, L. P. Assumed strain stabilization of the eight node hexahedral element. *Comput. Methods Appl. Mech. Eng.* **105**, 225–260. https://doi.org/10.1016/0045-7825(93)90124-G (1993).
36. Schwer, L. E., Key, S. W., Pucik, T. A. & Bindeman, L. P. An assessment of the LS-DYNA hourglass formulations via the 3D patch test. In Proceedings of the 5th European LS-DYNA users conference, 4c-05. (2005).
37. Blanchot, V. & Daidié, A. Riveted assembly modelling: Study and numerical characterisation of a riveting process. *J. Mater. Process. Technol.* **180**, 201–209. https://doi.org/10.1016/j.jmatprotec.2006.06.005 (2006).
38. Zhang, X. B., Zhao, X., Zhang, Y. M. & Li, Z. G. A one-point quadrature element used in simulation of cold ring rolling process. *Mater. Sci. Forum.* **704**, 165–171. https://doi.org/10.4028/www.scientific.net/MSF.704-705.165 (2012).
39. Stewart, J. R., Gullerud, A. S. & Heinstein, M. W. Solution verification for explicit transient dynamics problems in the presence of hourglass and contact forces. *Comput. Methods Appl. Mech. Eng.* **195**, 1499–1516. https://doi.org/10.1016/j.cma.2005.05.043 (2006).
40. Yang, G. T. *Introduction to Elastoplastic Mechanics* 252–253 (Tsinghua University Press, 2013).

Acknowledgements

We are grateful for the support of the National Key Research and Development Project (grant number 2019YFB1707505) and the Jilin Scientific and Technological Development Programs (grant number 20200401139GX and 20200401128GX).

Author contributions

P.L. conducted experiments and completed the writing of the manuscript; C.T. guided the experiment and the writing of the manuscript; P.L. and H.X. carried out simulation analysis; Z.Y. assisted in the experiment. G.L., P.W. and G.H. participated in the discussion of experimental and simulation data. All authors reviewed the manuscript.

Competing interests

The authors declare no competing interests.

Additional information

Correspondence and requests for materials should be addressed to C.T.

Reprints and permissions information is available at www.nature.com/reprints.

Publisher's note Springer Nature remains neutral with regard to jurisdictional claims in published maps and institutional affiliations.